Acta Oceanol. Sin., 2020, Vol. 39, No. 1, P. 14–24
https://doi.org/10.1007/s13131-019-1523-2
http://www.hyxb.org.cn
E-mail: hyxbe@263.net

Principal-component estimates of the Kuroshio Current axis and path based on the mathematical verification between satellite altimeter and drifting buoy data

Zhanpeng Zhuang[1, 2*], Zhenli Hui[1, 2], Guangbing Yang[1, 2], Xinhua Zhao[3], Yeli Yuan[1, 2]

[1] The First Institute of Oceanography, Ministry of Natural Resources, Qingdao 266100, China

[2] Laboratory for Regional Oceanography and Numerical Modeling, Qingdao National Laboratory for Marine Science and Technology, Qingdao 266237, China

[3] Institute of Oceanology, Chinese Academy of Sciences, Qingdao 266071, China

Received 12 December 2018; accepted 15 July 2019

Abstract

We used satellite altimetry data to investigate the Kuroshio Current because of the higher resolution and wider range of observations. In previous studies, satellite absolute geostrophic velocities were used to study the spatio-temporal variability of the sea surface velocity field along the current, and extraction methods were employed to detect the Kuroshio axes and paths. However, sea surface absolute geostrophic velocity estimated from absolute dynamic topography should be regarded as the geostrophic component of the actual surface velocity, which cannot represent a sea surface current accurately. In this study, mathematical verification between the climatic absolute geostrophic and bin-averaged drifting buoy velocity was established and then adopted to correct the satellite absolute geostrophic velocities. There were some differences in the characteristics between satellite geostrophic and drifting buoy velocities. As a result, the corrected satellite absolute geostrophic velocities were used to detect the Kuroshio axis and path based on a principal-component detection scheme. The results showed that the detection of the Kuroshio axes and paths from corrected absolute geostrophic velocities performed better than those from satellite absolute geostrophic velocities and surface current estimations. The corrected satellite absolute geostrophic velocity may therefore contribute to more precise day-to-day detection of the Kuroshio Current axis and path.

Key words: Kuroshio axis detection, Kuroshio path detection, mathematical verification, satellite absolute geostrophic velocity, principal-component detection

Citation: Zhuang Zhanpeng, Hui Zhenli, Yang Guangbing, Zhao Xinhua, Yuan Yeli. 2020. Principal-component estimates of the Kuroshio Current axis and path based on the mathematical verification between satellite altimeter and drifting buoy data. Acta Oceanologica Sinica, 39(1): 14–24, doi: 10.1007/s13131-019-1523-2

1 Introduction

The Kuroshio Current (KC) is the western boundary current in the wind-driven subtropical North Pacific Ocean gyre, and it transports huge amounts of heat and nutrients poleward (Qiu, 2001). Variations in the KC position often have a profound effect on hydrography, fishing industries and climate of countries in the northwestern Pacific region (Teague et al., 2003; Matsuno et al., 2009); therefore, the positions of the KC axis and path have been regularly monitored and include a huge amount of observational data (Ambe et al., 2004). Various remote sensing instruments, such as the altimeter, are designed to collect the sea surface height (SSH). Satellite altimetry has enabled us to obtain uniform sea surface topography over a wide area with high resolution. Assuming geostrophy, sea surface velocity can be obtained from the slope of the sea surface topography, which has been used to derive information about the KC such as axis and path.

In previous studies that used satellite altimetry data, spatio-temporal variability along the KC has been discussed. Imawaki et al. (1996) detected the fluctuations of the KC axis south of Japan using sea surface dynamic topography from TOPEX/POSEIDON altimeter data from 1992–1993. Liu and Gan (2012) investigated spatial and temporal surface variability of the axis, width, along and cross-stream transports of the entire KC in the East China Sea using 16-year (1993–2008) surface geostrophic currents derived from satellite altimetry data. However, the sea surface geostrophic velocity estimated from SSH can be regarded as the geostrophic component of the actual surface velocity (Lagerloef et al., 1999; Arbic et al., 2012), which cannot represent the sea surface current accurately. There is an obvious deviation between the KC axes extracted from satellite altimetry and drifting buoy data using the extraction method of Ambe et al. (2004) (Fig. 1).

Additionally, the surface velocities have been estimated by combining in situ drifting buoy velocities with velocity anomalies derived from altimeter sea level anomaly data (Uchida and Imawaki, 2003). The instantaneous velocities agree well with in situ surface velocities; however, the temporal resolution was 10 days because of a lack of drifting buoy observations. In this study, the absolute geostrophic velocity (AGV) was corrected and was

Foundation item: The National Science and Technology Major Project of the Ministry of Science and Technology of China under contract No. 2018YFF01014100; the National Programme on Global Change and Air-Sea Interaction under contract No. GASI-IPOVAI-01-05; the NSFC-Shandong Joint Fund for Marine Science Research Centers under contract No. U1606405.
*Corresponding author, E-mail: zhuangzp@fio.org.cn

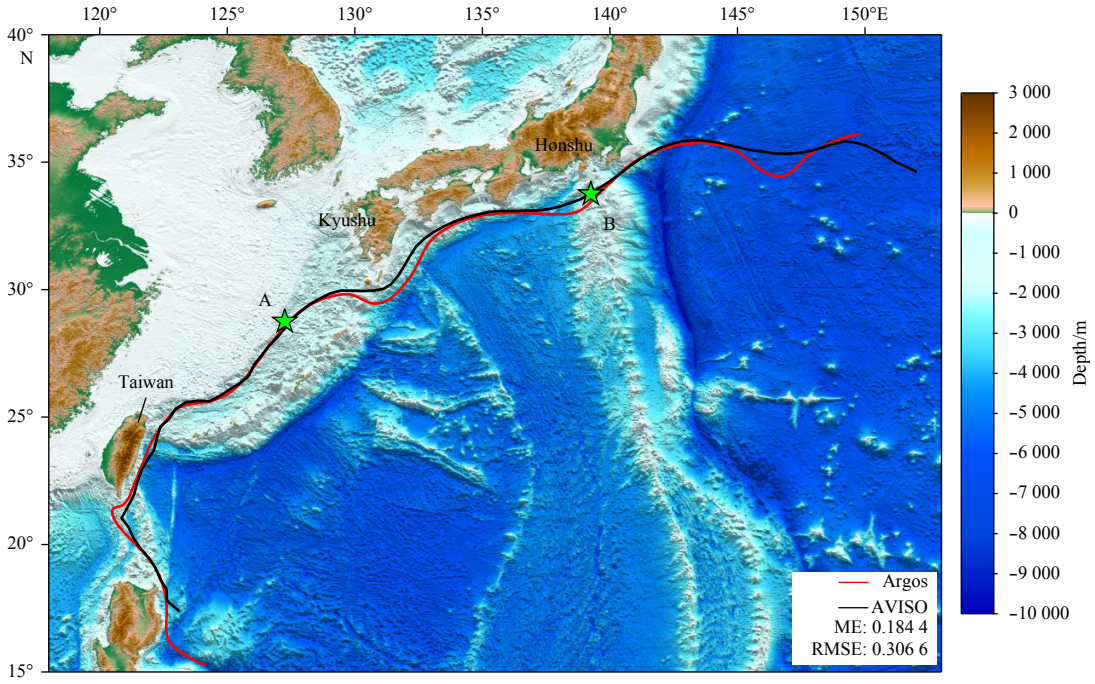

Fig. 1. The study region with bathymetry. Climatic information of the Kuroshio Current is derived from the yearly averaged results from 1993–2017 merged with absolute geostrophic (blue line) and 38 a (1979–2016) Argos drifting buoy (red line) velocities. The mean error (ME) and root mean square error (RMSE) between these two lines were calculated. Two representative points (green stars), located at 28.75°N, 127.25°E (Point A) and 33.75°N,139.25°E (Point B), were chosen to show the fitting functions at the coefficient grids. The scatter diagrams are shown in Fig. 4.

found to be closer to actual surface velocities. This method is more direct, accurate and simpler. The temporal resolution was one day, the same as the satellite altimetry data distributed by the Copernicus Marine Environment Monitoring Service (CMEMS).

An extraction scheme for detecting the KC axis and path based on principal-component analysis is described in great detail. Mathematical verification, which is used to correct the satellite altimetry data, of the geostrophic and actual surface velocity was established using a linear numerical fitting algorithm. Based on the altimetry data corrected by this determined relationship, the KC axes and paths were extracted more accurately.

2 Data

2.1 *Surface geostrophic velocity*

A 25 a (1993–2017) time series of merged AGV data was used in this study. The data are now distributed by CMEMS and derived from the Ssalto multi-mission ground segment/data unification and altimeter combination system (Ssalto/Duacs) processing that integrated data from all altimeter missions (HY-2A, Saral/AltiKa, Cryosat-2, OSTM/Jason-2, Jason-1, Topex/Poseidon, Envisat, GFO and ERS-1&2) (CNES, 2016). The AGV was calculated from the absolute dynamic topography, which is the sum of the sea level anomaly and the mean dynamic topography, using the 9-point stencil width method (Arbic et al., 2012). In this study, the AGV data were corrected based on the drifting buoy velocity fields, then used to detect the KC axes and paths.

2.2 *Argos drifting buoys*

The trajectory data are provided by Argos, which is a satellite-based system that collects, processes and disseminates environmental data from fixed and mobile platforms worldwide. A total of 4 710 Argos drifters, of which the drogue is generally placed at a depth of 15 m, in the study area of 15°–40 °N, 116°–153°E (Fig. 1) and from 1979 to 2016 are used. The observations mainly include position, velocity and temperature with a 6 h interval, and the observation deviation of the velocity caused by positioning errors is less than or equal to 5 cm/s approximately (Ishikawa et al., 1997), therefore, the surface current derived from these drifter data can

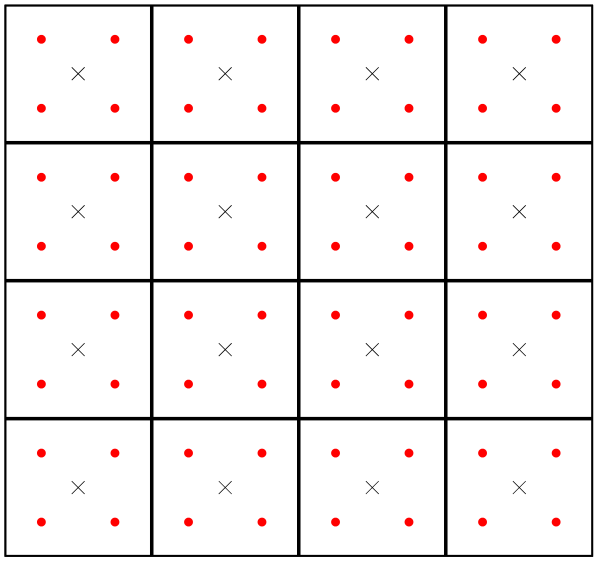

Fig. 2. Distribution diagram of the data and coefficient grids. The red points denote the centers of the data grids and the black crosses indicate the coefficient grid centers represented as black solid lines.

be considered authentic.

After implementing quality control and removing the abnormal points, the velocity records are first segregated into geographic bins of (1/4)° × (1/4)° (Hu et al., 2008). The bin that only contain less than or equal to three records will be regarded as invalid one and deleted. For each of the valid bins, which contains more than three records, the velocity in the center of the bin is interpolated from all of the records in this bin using the inverse distance weighted (IDW) algorithm, of which the expression can be represented as

$$\hat{z}(x_0, y_0) = \sum_{i=1}^{n} \frac{1/d_i}{\sum_{i=1}^{n} 1/d_i} \cdot z(x_i, y_i), \tag{1}$$

where $\hat{z}(x_0, y_0)$ denotes the interpolated value in the center, $z(x_i, y_i)$ represents the ith record, d_i is the distance from the position of the ith record to the center of the bin. When the inverse distance weighted algorithm is applied, it ensures that the shorter the distance from the center, the greater the weight. As a reference, the bin-averaged drifting buoy velocities (DBV) are regarded as the true value to validate other velocities because they are calculated from in situ observations.

2.3 *Surface current estimation*

According to the analyses of Lagerloef et al. (1999) and Hui and Xu (2016), the surface current estimate (SCE) was calculated in this study. The SCE from 1993 to 2017 was calculated as the sum of the geostrophic velocities from SSH, Ekman velocity from wind stress and the Stokes drift estimated from the surface wave data (Hui and Xu, 2016):

$$\boldsymbol{U} = \boldsymbol{U}_g + \boldsymbol{U}_e + \boldsymbol{U}_w, \tag{2}$$

where $\boldsymbol{U}$ denotes the SCE. $\boldsymbol{U}_g = \left(-\frac{g}{f}\frac{\partial \xi}{\partial y}, -\frac{g}{f}\frac{\partial \xi}{\partial x}\right)$ is the geostrophic velocity and the same as that mentioned in Section 2.1 in which f=2Ωsinφ is the Coriolis parameter, Ω is the rotation angular velocity of the Earth and φ is the angle of latitude, g is the gravitational acceleration and ξ is the SSH. $\boldsymbol{U}_e = B\mathrm{e}^{i\theta}\left(\tau_x + i\tau_y\right)$ is the Ekman current calculated from the classical Ekman model (Wu and Liu, 2008), where $B \approx 0.3$ m/(s · Pa) is the amplitude coefficient in the northwestern Pacific Ocean, θ=55° is the turning angle relative to the wind direction in the northern hemisphere. $\boldsymbol{U}_w = -\frac{2kj\boldsymbol{U}_s(0)}{(2k)^2 - j^2} \cdot \mathrm{e}^{jz} + \frac{j^2\boldsymbol{U}_s(0)}{(2k)^2 - j^2} \cdot \mathrm{e}^{2kz}$ is the wave-modified term that denotes the wave-induced Coriolis-Stokes forcing and calculated based on the equation given by Philipps (1977), where $\boldsymbol{U}_s(z) = \frac{2\pi^3 H_s^2}{gT^3} \mathrm{e}^{\frac{8\pi^2}{gT^2}z} \cdot \vec{\boldsymbol{k}}$ is the Stokes drift velocity at the sea surface, H_s is the significant wave height, T is the mean wave period, $\vec{\boldsymbol{k}}$ is the unit wavenumber vector, $k = \frac{4\pi^2}{gT^2}$, $j = (1+i)/d$ when $d = \sqrt{2A_Z/f}$ and $A_Z = 1.2 \times 10^{-4}\left(u_{10}^2 + v_{10}^2\right)$ is the vertical eddy viscosity, u_{10} and v_{10} are zonal and meridional wind speed components at 10 m above the sea surface. In this study, the European Centre for Medium-Range Weather Forecasts (ECMWF) interim surface wave and wind data of 1993–2017 were used to estimate the Ekman velocities and Stokes drift, then the surface velocities in the same time intervals were calculated as the sum of these components. The details of deriving and calculating processes of the Ekman velocity and Stokes drift were introduced in Lagerloef et al. (1999) and Hui and Xu (2016), respectively.

2.4 *Ocean current time series data*

A time series of the day-to-day current maps from 1–31 January 2016 were used to examine the accuracy of the detection results of KC paths based on AGVs and corrected AGVs. The maps were provided by the Hydrographic and Oceanographic Department of Japan based on in-situ observations. Geographic information data processing software, such as ArcGIS, were used to obtain day-to-day KC paths from GIS data (shape files) of the streamlines.

3 Algorithm description

3.1 *Seasonal, semi-yearly and yearly averaged algorithm*

The seasonal, semi-yearly and yearly climate data of velocities, calculated as averages of the records in all of the years, included satellite AGV, bin-averaged DBV and SCE. Thus, these climatology results can be seen as the averaged statistical time windows including four seasons, two semi-years (winter was from October to March and summer was from April to September) and one year. It is worth noting that the data records from the Argos drifter are very scarce and actually not enough to cover the entire study area from 1993 to 2016. The climatology averages exhibit a mean spatial distribution of the KC if the time interval is very long. Therefore, there is little difference in the seasonal, semi-yearly and yearly climatology results between the 25 a AGV (1993–2017) and the 37 a DBV (1979–2016).

3.2 *Mathematical verification*

The spatial resolution of the altimetry data and the preprocessed bin-averaged results was the same, so this ensured that the grid points of these two types of data were at the same locations. To obtain the corrected AGV, the numerical fitting method builds a relationship between the climate satellite AGV and bin-averaged DBV based on the least square method (LSM). The LSM is a procedure to determine the best fit line to data, which often means that the sum of the distance from all of the points to this line is the least value. The relationship is represented as:

$$V_{\mathrm{db}} = k \times V_{\mathrm{sg}} + b, \tag{3}$$

where V_{db} and V_{sg} denote the drifting buoy and satellite geostrophic velocities, respectively, and k and b represent the fitting coefficients. To minimize the square of the error term and obtain the best k and b, the expression is:

$$E^2 = \sum_{n=1}^{N} \left(V_{\mathrm{db}\,n} - k \cdot V_{\mathrm{sg}\,n} - b\right). \tag{4}$$

Differential calculus was used to take the partial derivative of Eq. (2) with respect to k and set it equal to zero; the same was done with respect to b. The system of equations with two unknowns, k and b, was solved, and the solutions shown as:

$$k = \frac{\sum_{n=1}^{N}\left(V_{\mathrm{db}\,n} - \bar{V}_{\mathrm{db}}\right)\left(V_{\mathrm{sg}\,n} - \bar{V}_{\mathrm{sg}}\right)}{\sum_{n=1}^{N}\left(V_{\mathrm{db}\,n} - \bar{V}_{\mathrm{db}}\right)^2}, \tag{5}$$

$$b = \bar{V}_{\mathrm{db}} - \frac{\sum_{n=1}^{N} \left(V_{\mathrm{db}\,n} - \bar{V}_{\mathrm{db}}\right)\left(V_{\mathrm{sg}\,n} - \bar{V}_{\mathrm{sg}}\right)}{\sum_{n=1}^{N} \left(V_{\mathrm{db}\,n} - \bar{V}_{\mathrm{db}}\right)^2} \cdot \bar{V}_{\mathrm{sg}}, \tag{6}$$

where $\bar{V}_{\mathrm{db}} = \sum_{n=1}^{N} \left(\frac{1}{N} \cdot V_{\mathrm{db}\,n}\right)$ and $\bar{V}_{\mathrm{sg}} = \sum_{n=1}^{N} \left(\frac{1}{N} \cdot V_{\mathrm{sg}\,n}\right)$ denote the mean values.

To obtain a relatively accurate relationship, the geostrophic components and actual surface velocities in the local small area do not vary greatly, but the number of grid points used needs to be sufficient. Therefore, all of the grid points in the study area were further segregated into bins of (1/2)° × (1/2)° called coefficient grids (Fig. 2). In other words, each of these grids contains four original grid points, in which a unique linear fitting function was obtained using the LSM. For each of the coefficient grids, the climatology results in three different statistical time windows including two semi-years and one year were used to establish the relationship. The seasonal climatology results were not used because of the higher number of invalid grids, but these results were used for validation (see Section 4). This implies that there are, at most, 12 DBV data records in a coefficient grid, but these DBV data are missing for the invalid original grids. There are few invalid grids for yearly and semi-yearly data, so there are 10 or more DBV data records in most of the coefficient grids. However, because the measuring accuracy of the drifting buoys is relatively low when the values of the measurements are small, the DBV data records cannot be used for a fitting function if the absolute value is less than 0.2 m/s. Additionally, if the number of DBV data records are less than or equal to three, the data are too few to establish a linear fitting relationship because the accuracy cannot be satisfied. In other words, the fitting functions in these coefficient grids are missing, corresponding to the blank regions in Fig. 5.

Based on the fitting functions, the satellite AGVs can be corrected as:

$$V_{\mathrm{ag}\,i,j} = k_{I,J} \times V_{\mathrm{sg}\,i,j} + b_{I,J}, \tag{7}$$

where $V_{\mathrm{ag}\,i,j}$ and $V_{\mathrm{sg}\,i,j}$ denote the corrected and original satellite AGV, respectively, at grid point (i, j) and $k_{I,J}$ and $b_{I,J}$ are the slope and intercept of the linear fitting function, respectively, at the corresponding (I, J) coefficient point.

3.3 *Extraction of Kuroshio Current axes and paths*

The positions of the KC axes were estimated by tracking the locally strongest part of the sea surface velocity in the subsidiary lines. The detection method was established according to Ambe et al. (2004) and the selection of several parameters was specific. Figure 3 depicts the calculation of the KC axis and path. Along each of the subsidiary lines, the local maximum velocity (V_0) corresponds to the KC axis, and the velocities often decrease gradually from the axis to two sides. In this study, the length of a subsidiary line was 140 km. The velocities were interpolated to the points of the subsidiary lines, and the interval between two adjacent points was 7 km. A subsidiary line moves downstream along the local maximum velocity (V_0) to the next location and is adjusted to be perpendicular to the direction of the new V_0. The distance the subsidiary line moves downstream was 10 km. The KC paths were determined by shore-side and sea-side boundaries (P and Q in Fig. 3), in which the velocities (V_u and V_d) became less than the cut-off velocity for the first time of travel from the axis to two sides along the subsidiary line. The cut-off velocities were 20% of V_0 with consideration of one-sidedness when they were constants.

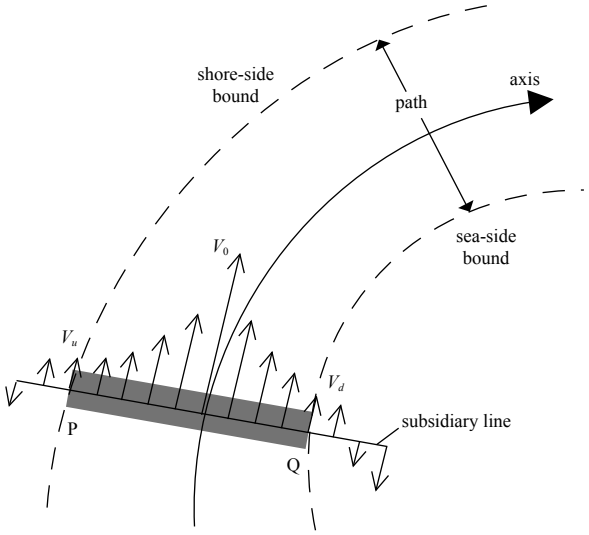

Fig. 3. Schematic of the axis, shore-side and sea-side boundaries, subsidiary line, maximum velocity at the axis (V_0) and boundary velocities (V_u and V_d).

4 Algorithm implementation and validation

The DBV was derived from successive locations of drifters at 15 m, which was the in-situ observation. However, the AGV noted the geostrophic velocity at the sea surface. So there was a slight discrepancy between DBV and AGV. In this study, we focused on data extraction for KC axes and paths, and the small depth difference between DBV and AGV was ignored.

4.1 *Mathematical verification*

The yearly and semi-yearly climate data from satellite AGV and bin-averaged DBV were used to establish the mathematical verification. Figure 4 presents the linear fitting functions in two bins with centers located at 28.75°N,127.25°E (Point A) and 33.75°N, 139.25°E (Point B). Point A is located in a straight part of the Kuroshio region southwest of the East China Sea, and Point B is located south of Honshu Island with the KC path characterized by alternating large and small meanders (Qiu, 2001; Miyazawa et al., 2008). The fitting function at Point A is obviously closer to a linear relationship because the velocities are more stable compared with Point B (Fig. 4).

The spatial distribution of the slope k and intercept b of the linear fitting relationship with horizontal resolution of (1/2)° × (1/2)° in the whole study area is shown in Fig. 5. In the open ocean located to the south of the KC, the central and northern parts of the East China Sea, the Yellow Sea and the Sea of Japan, the linear fitting functions almost could not be obtained (Fig. 5) because the absolute value of DBV was less than 0.2 m/s. However, these regions are all out of the KC paths and not a major concern in this study, so it was acceptable to ignore these regions. In addition, the linear fitting functions for the meridional component v are missing in the KC regions south of Japan and some areas of the Kuroshio Extension Area because the KC in these regions flows mainly from west to east, so the absolute value of v was often less than 0.2 m/s (Figs 5c–d).

In all of the regions where the fitting functions are missing,

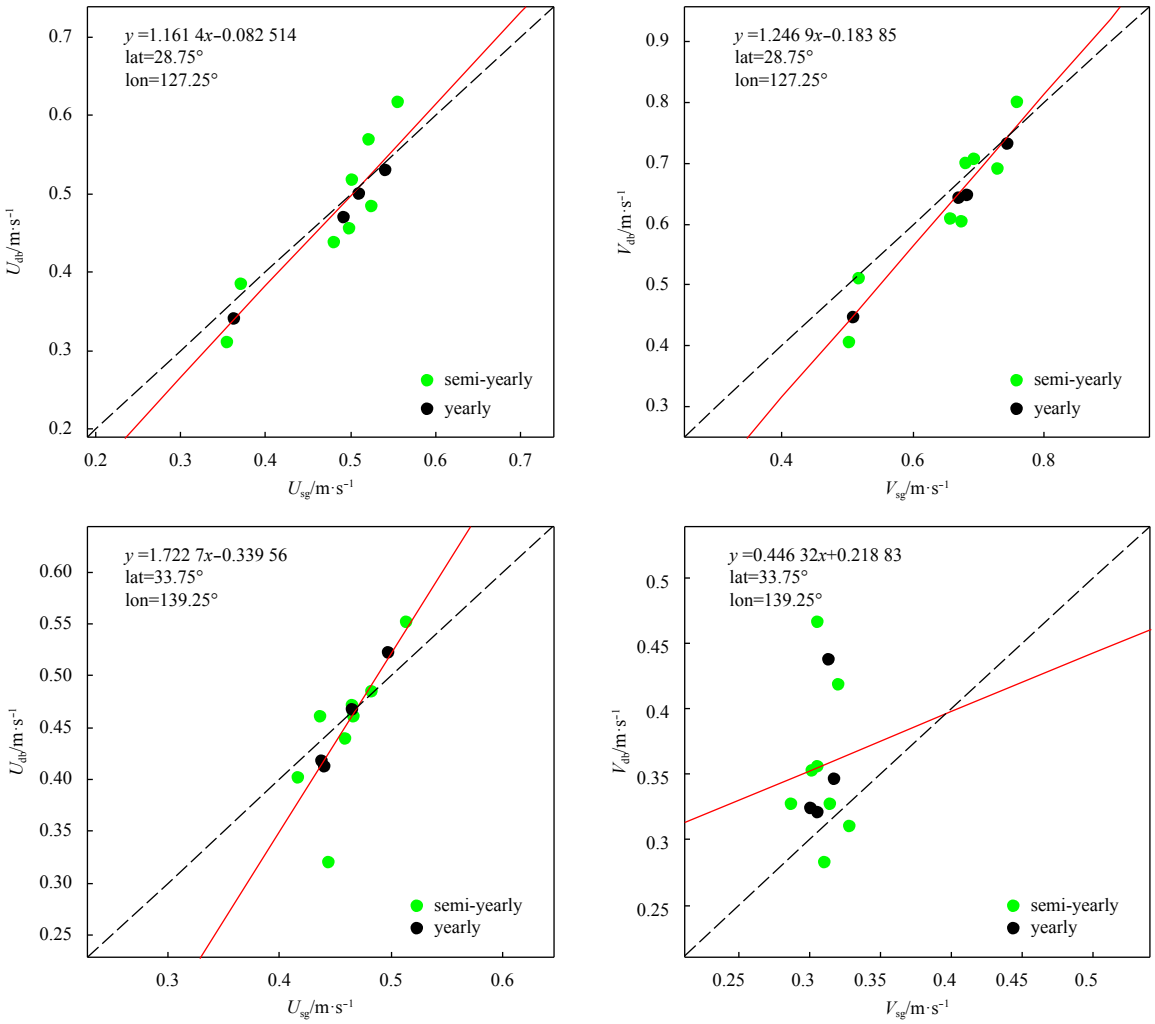

Fig. 4. Scatter diagrams of the satellite geostrophic velocities versus drifting buoy velocities, including zonal component U (left panels) and meridional component V (right panels); the red solid lines indicate the linear relationship between the two results. As a reference, the black dashed lines denote standard lines corresponding to y=x. In the top left portions of each panel, the linear relationship equation is shown along with the longitude and latitude corresponding to the center of the (1/2)° × (1/2)° coefficient grids.

the AGVs were not corrected, so the relationship should be regarded as k=1 and b=0. The spatial distribution of k and b corresponds to the regions in which the difference between the satellite AGV and bin-averaged DBV was large (Figs 6a and d). Furthermore, the k and b southwest of the East China Sea are closer to 1 and 0, respectively, than in other KC regions. It is worth noting that in the Kuroshio regions some other factors, such as different bottom topography, coastline geometry, surface wind patterns and sea waves (Lagerloef et al., 1999; Qiu, 2001), may play an important role in the detection of the KC axis and path. The verification between the AGV and bin-averaged DBV proposed in this study may suggest other factors, and further support and calibration from theoretical studies and field observations is needed to make the corrected AGVs more accurate.

4.2 *Validation of the Kuroshio axes and paths detection*

The seasonally averaged results of the AGVs (U_{sg}), SCEs (U_{se}) and corrected AGVs (U_{ag}) are compared with the bin-averaged DBVs (U_{db}) in summer and winter (Fig. 6). The U_{db} was regarded as observations. The difference in the KC regions for these three classes of surface velocity was relatively larger than in the open ocean south of the KC and the Sea of Japan. In summer, the U_{sg} and U_{se} were 0.3–0.6 m/s slower than the U_{db} southwest of Kyushu Island, south of Honshu Island (~135°–140°E), and the eastern regions of Japan (~142°–145°E) and 0.1–0.4 m/s faster in the KC regions between ~133°E and 138°E and ~145°E and 150°E (Figs 6a–c). The differences of U_{sg}–U_{db} and U_{se}–U_{db} were relatively small (±0.1 m/s) east of Taiwan and in the southwestern East China Sea.

The mean error (ME) and root mean square error (RMSE) were calculated to assess the difference quantitatively. The ME is the arithmetic mean of the error values and the RMSE is the square root of the mean of squared errors. In summer, the ME for U_{ag} was the smallest, but the RMSE for U_{ag} was larger than U_{sg}, which implies that the fluctuation in differences between U_{sg} and U_{db} was smaller than U_{ag}. On the whole, the MEs and RMSEs for U_{sg}, U_{se} and U_{ag} were very similar.

Similar to summer, the spatial distribution of differences in winter was analyzed (Figs 6d–f). The U_{sg} and U_{se} were 0.4–0.6 m/s faster than the U_{db} in the KC region between ~130°E and 132°E, and 0.3–0.6 m/s slower south of Honshu Island between ~135°E and 140°E. The difference between U_{ag} and U_{db} was obviously

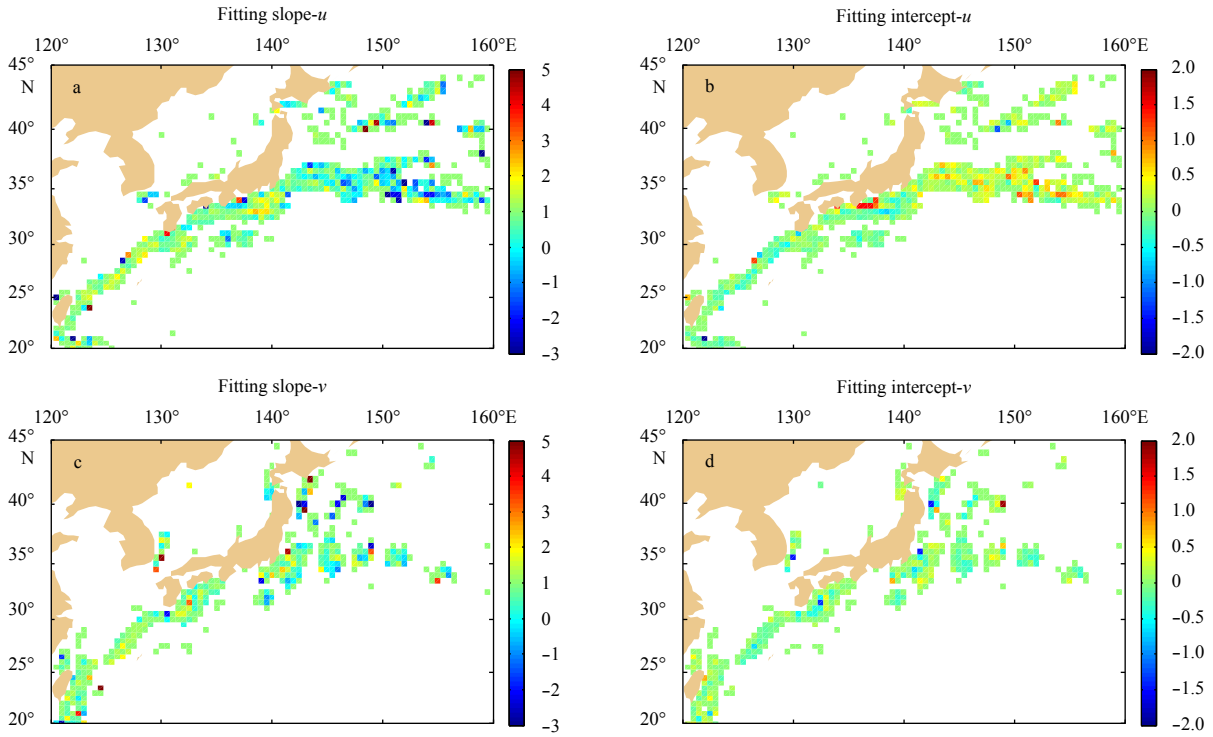

Fig. 5. Spatial distribution of the Kuroshio Current velocities linear relationship, including the slope (a, c) and intercept (b, d), of the fitting lines. a and b denote the zonal components of the velocities while b and d indicate the meridional components. The blank regions (white areas) represent areas where the mathematical relationship could not be established.

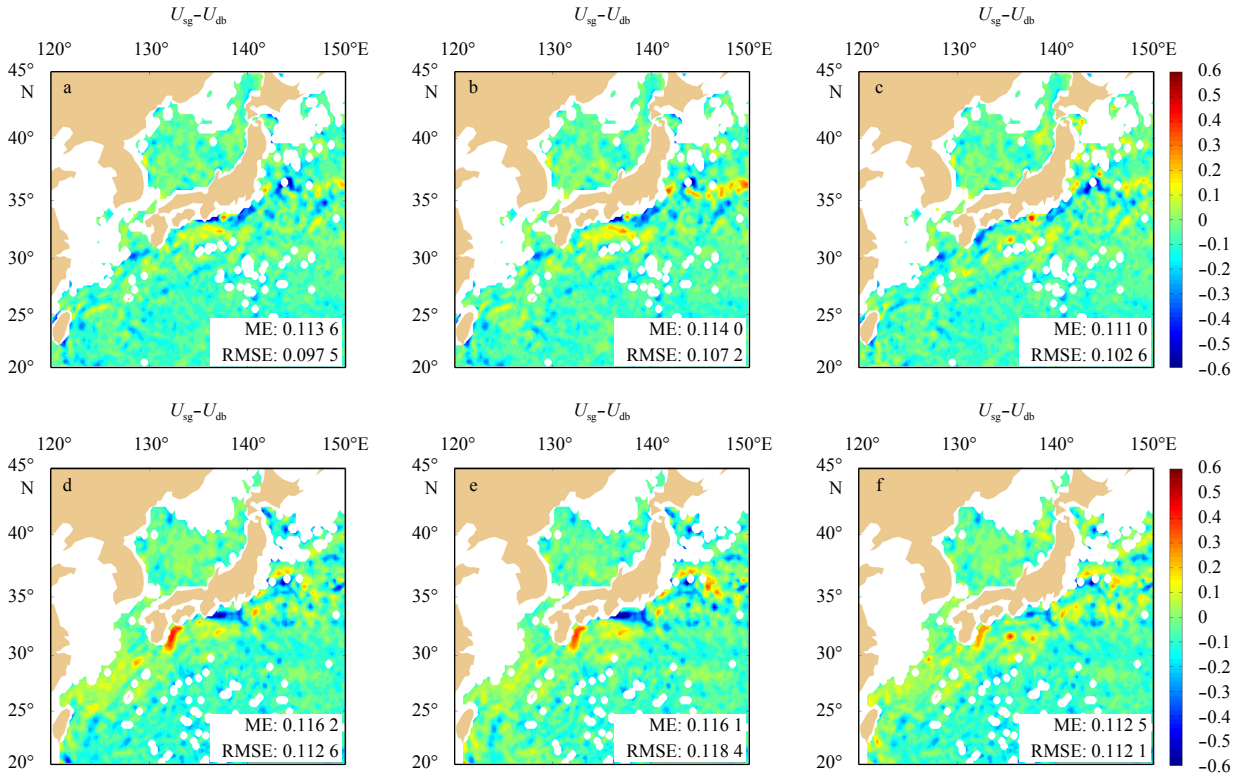

Fig. 6. Difference of the surface velocity fields (m/s) calculated by subtracting the satellite geostrophic (U_{sg}) and corrected satellite geostrophic (U_{ag}) velocities and surface current estimates (U_{se}) from the bin-averaged drifting buoy velocities (U_{db}). The mean error (ME, m/s) and root mean square error (RMSE, m/s) are shown. The top and bottom panels correspond to the summer and winter seasonal averaged results, respectively. The blank regions (white areas) correspond to the invalid grids of the U_{db} fields.

smaller than U_{sg} and U_{se} in these regions. In the KC region east of Japan (~144°–150°E), the difference between U_{ag} and U_{db} was –0.3 m/s to 0.2 m/s, which was also smaller than U_{sg} and U_{se}. Therefore, the ME and RMSE for U_{ag} in winter were somewhat smaller than U_{sg} and U_{se}.

There was not a noticeable improvement in corrected AGVs with the proposed mathematical verification because U_{ag} was not closer to U_{db} compared with U_{sg} and U_{se} (Fig. 6). Therefore, the KC axes and paths detected from U_{sg}, U_{se} and U_{ag} were compared directly to assess the effect of verification. The KC axes and paths detected from U_{db} were still regarded as the reference.

The KC axes and paths for U_{ag} are closer to U_{db} compared with U_{sg} and U_{se} in the southwestern and southern regions off Kyushu Island and the Kuroshio Extension Area (Figs 7 and 8). The ME, RMSE and correlation coefficients (CCs) were calculated to show the difference quantitatively. The CCs ranged from –1 to 1, where 1 indicates the strongest agreement and –1 the strongest disagreement. The MEs and RMSEs of the KC axes and paths between U_{ag} and U_{db} were the smallest, and the CCs were closer to 1 than the other two types of surface velocity fields (Fig. 9). The extraction accuracy based on U_{ag}, therefore, was remarkably improved compared with U_{sg} and U_{se}. There is no obvious improvement to detect the KC axis and path for U_{se} because those detected from U_{sg} and U_{se} almost coincided (Figs 7 and 8), and the MEs, RMSEs and CCs for U_{sg} and U_{se} were almost equal (Fig. 9). This implies that the proposed mathematical verification is able to detect more accurate KC axes and paths when it is used to correct the seasonal climatology data of satellite AGVs.

The MEs, RMSEs and CCs of the detected KC axes were best in summer and worst in autumn, while the KC path parameters

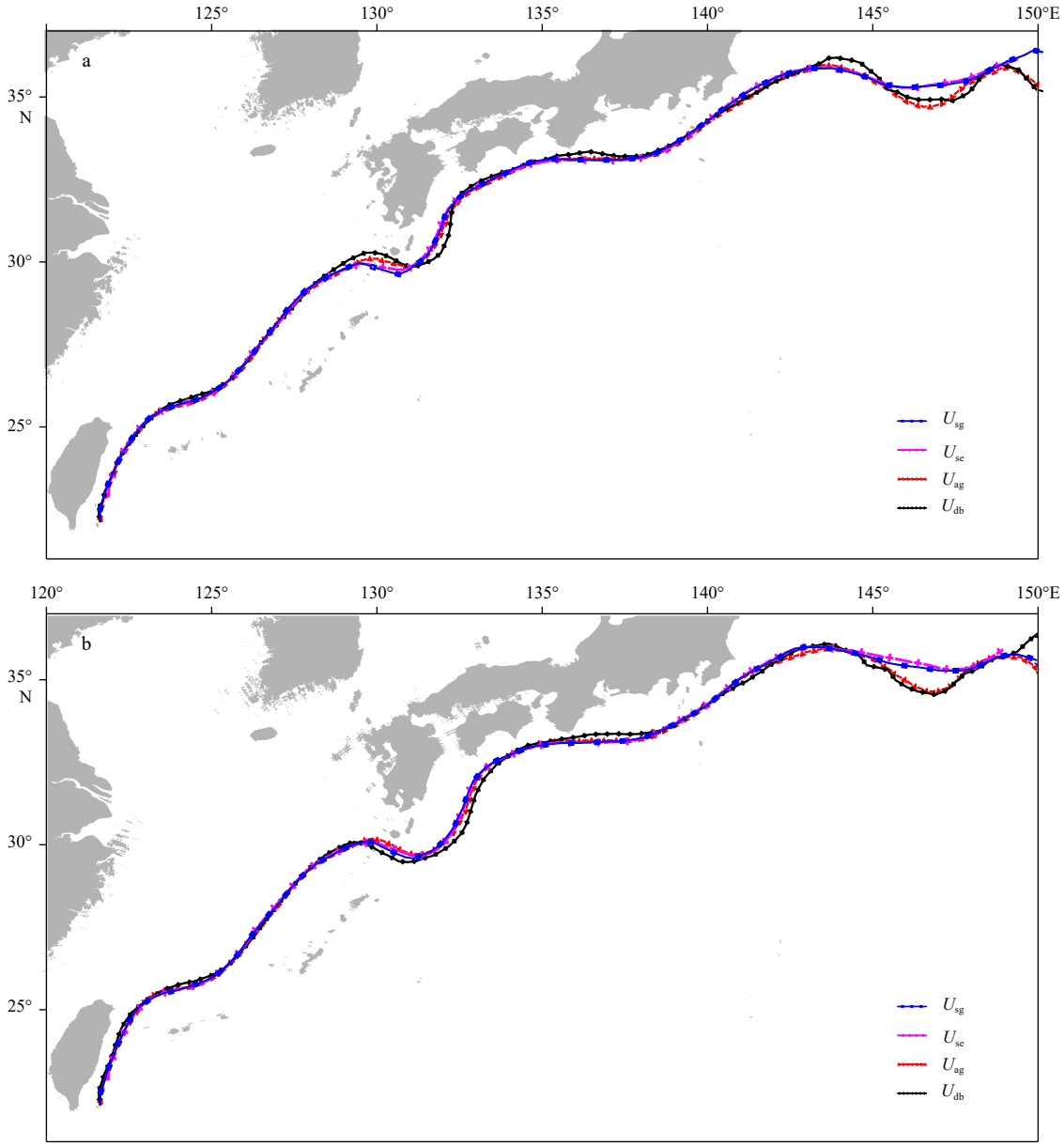

Fig. 7. Distribution of the seasonal averaged locations of the Kuroshio Current axes in (a) summer and (b) winter based on four different surface velocity fields, including satellite absolute geostrophic velocities (AGVs, blue line with solid symbols), surface current estimates (magenta line with cross symbols), corrected satellite AGVs (red line with triangle symbols) and the bin-averaged drifting buoy velocities (DBVs, black line with diamond symbols).

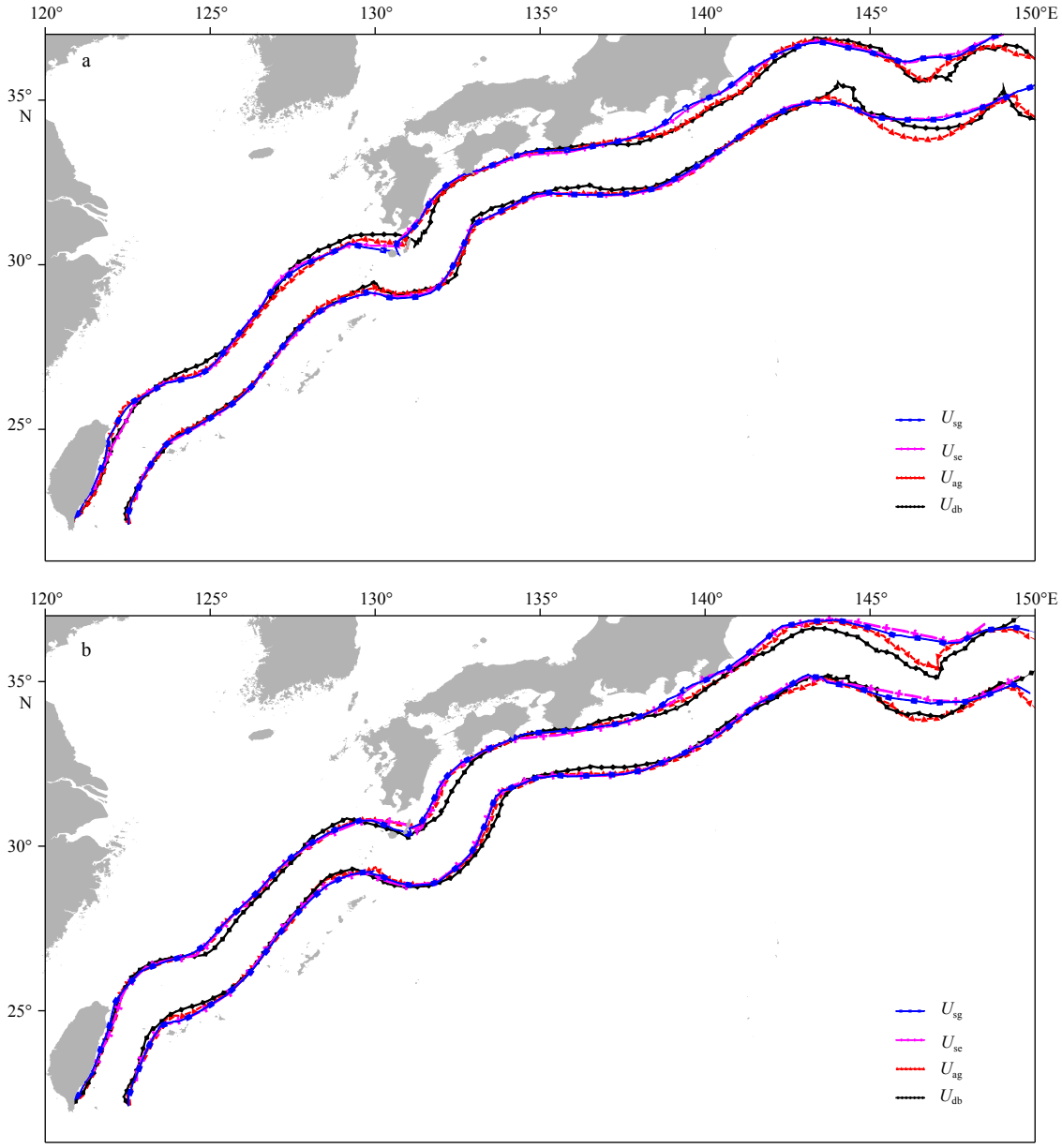

Fig. 8. Distribution of the seasonal averaged locations of the Kuroshio Current paths in summer (a) and winter (b) based on four different surface velocity fields, including satellite absolute geostrophic velocities (AGVs, blue line with solid symbols), surface current estimates (magenta line with cross symbols), corrected satellite AGVs (red line with triangle symbols) and the bin-averaged drifting buoy velocities (DBVs, black line with diamond symbols).

were best in autumn and worst in winter (Fig. 9). This may be because the KC axis and path detected from a U_{db}-based extraction method becomes less well-organized, especially in the Kuroshio Extension Area. Furthermore, seasonal differences may be related to variability in the surface current fields (Hu et al., 2008). In the east and northeast regions off Taiwan, the KC is relatively stable in summer, but an intrusion onto the shelf is very obvious in autumn. In southwestern regions of Kyushu, the northward intrusion or breaching of KC surface water occurs mainly in spring, autumn and winter (it is not clear in summer). Therefore, the instability of the surface current field may also affect the path and axis detected from AGVs and then parameters such as MEs, RMSEs and CCs. In future work, some new in situ observations of the surface velocities are needed because there are still some errors between the bin-averaged DBVs and the actual flow velocities, and the parameters of the extraction method will be further optimized based on more experiments, observations and analysis.

4.3 *Validation of the daily Kuroshio path*

The day-to-day detection of the KC paths based on AGVs and corrected AGVs were compared daily reported data. The GIS data of the streamlines (U_{ja}) from the daily marine current maps in January 2016 were chosen and regarded as a reference. The day-to-day detection from the SCEs must be ignored because the detection of KC paths is usually influenced by meso-scale motion that enters the Sea of Japan or the open ocean located south of the KC.

From Fig. 10 one can see that There is an obvious difference

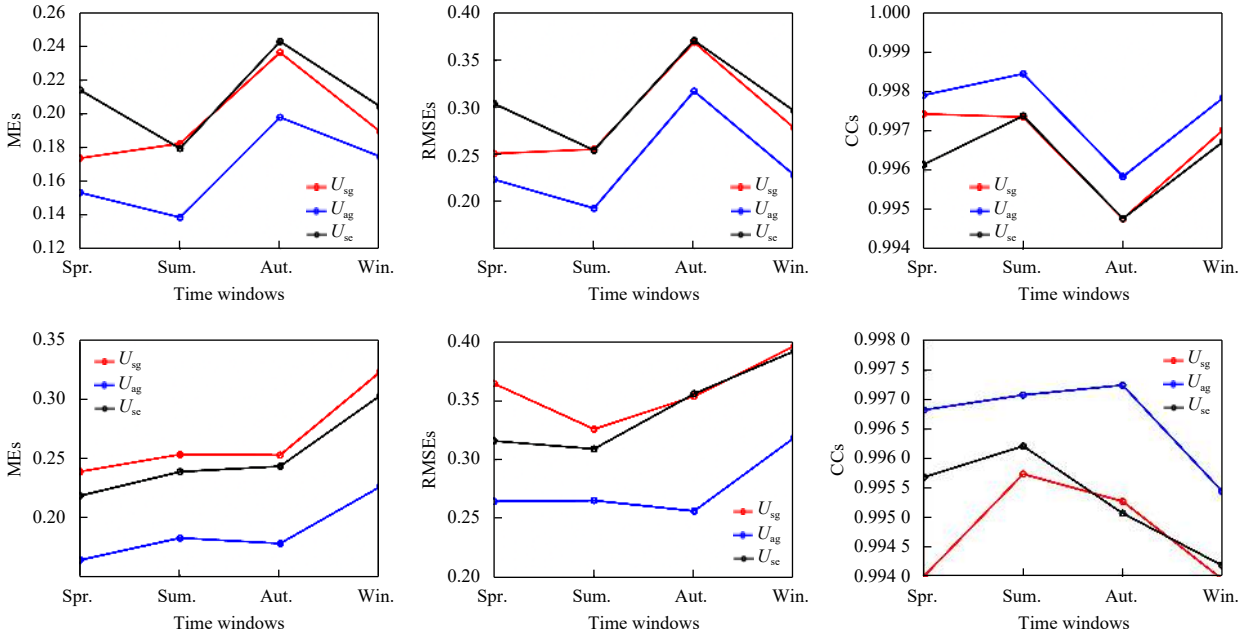

Fig. 9. The mean errors (MEs, left panels), root mean square errors (RMSEs, middle panels) and correlation coefficients (CCs, right panels) of the detected KC axes (first row) and paths (second row) were calculated between U_{sg} and U_{db} (red lines), U_{ag} and U_{db} (blue lines), and U_{se} and U_{db} (black lines) corresponding to four seasonal averaged results, including spring (Spr.), summer (Sum.), autumn (Aut.) and winter (Win.).

between the KC paths detected from U_{sg} and U_{ja}, and those from U_{ag} and U_{ja} east of Taiwan (~122°–124°E), south of Honshu Island (~139–142°E) and east of Japan between 145°E and 150°E. In the regions east of Taiwan, the KC paths detected from U_{sg} and U_{ag} were wider than U_{ja} because the velocity front in the KC boundary is not distinct and the KC paths may be estimated at more outside positions. Compared with U_{sg}, the KC paths detected from U_{ag} are closer to U_{ja} in the Kuroshio Extension Area, but in other regions there is no obvious improvement. Therefore, some indexes including MEs, RMSEs and CCs are calculated to comparing these results further.

Fig. 11 shows the comparisons of MEs, RMSEs and CCs between U_{sg} and U_{ja} and between U_{ag} and U_{ja} in all of January recorded in daily current maps. The three indices are almost the same in half of the days, and those for U_{ag} are slightly better than U_{sg} in most of the remaining days. Therefore, the day-to-day detection of the KC paths is somewhat improved by the proposed mathematical verification. The MEs, RMSEs and CCs of the detected KC paths were worse from 4–5 January, 14–15 January and 18–20 January (Fig. 11). This may reflect the obvious difference between the KC paths from U_{sg} and U_{ag} and those from U_{ja} because of the formation of the KC large meander southeast of Honshu Island and in the Kuroshio Extension Area. In future work, principal-component detection will be further optimized and contribute to more precise day-to-day detection of the KC axis and path.

5 Conclusions

Based on satellite AGV, the KC axes and paths were detected using some extraction methods in many previous studies. However, the sea surface geostrophic velocity estimated from SSH can be regarded as the geostrophic component of the actual surface velocity, which cannot represent the sea surface current accurately in the practical application. With the help of the linear numerical fitting algorithm, a mathematical verification between AGV and bin-averaged DBV was established and then used to correct the satellite altimetry data. The spatial distribution of the slope and intercept of the linear fitting relationship in the study area were analyzed. The regions with larger slope or intercept may indicate some other factors that could play an important role in affecting the detection of the KC axis and path. The seasonal climatology averaged results of the AGVs, SCEs and corrected AGVs were compared with the bin-averaged DBVs in summer and winter. The results showed that both of the surface velocity fields and the detected KC axes and paths for corrected AGVs performed the best compared with AGVs and SCEs. Furthermore, the day-to-day detection results of the KC paths based on AGVs and corrected AGVs were compared with daily current maps. Compared with AGVs, the day-to-day detection of the KC paths from corrected AGVs was improved. These corrected satellite AGVs may contribute to more precise day-to-day forecast of the KC axis and path.

Acknowledgements

We thank the anonymous reviewers for their careful reviews and constructive comments in improving the original manuscript, and the editors who kindly polished this article with great effort. The merged AGV remote sensing data were provided by CMEMS, and can be downloaded from ftp://ftp.aviso.altimetry.fr/. The QuikSCAT wind data were processed and distributed by the Centre ERS d'Archivage et de Traitement (CERSAT) and can be downloaded from ftp://ftp.ifremer.fr/ifremer/cersat/products/gridded/MWF/L3/QuikSCAT/Daily. The Interim surface wave data sets can be downloaded from the ECMWF link: http://apps.ecmwf.int/datasets/data/interim-full-daily/. The GIS data of the streamlines from the Hydrographic and Oceanographic Department of Japan can be downloaded from http://www1.kaiho.mlit.go.jp/KANKYO/KAIYO/qboc/kur-

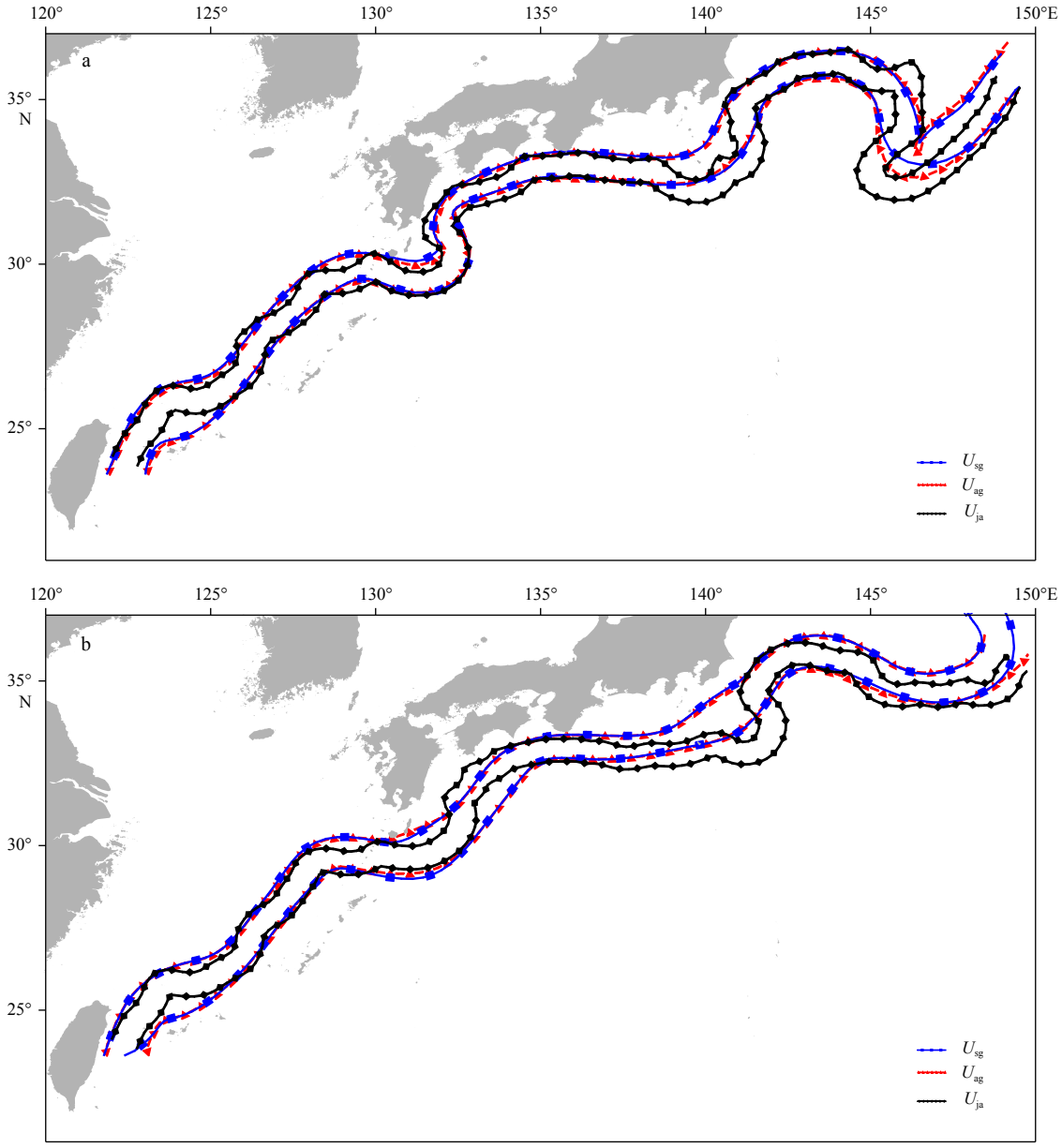

Fig. 10. Distribution of the Kuroshio Current paths on 4 January 2018 (a) and 20 January 2018 (b) based on satellite AGVs (blue line with square symbols), corrected satellite AGVs (red line with triangle symbols) and daily current maps (black line with diamond symbols).

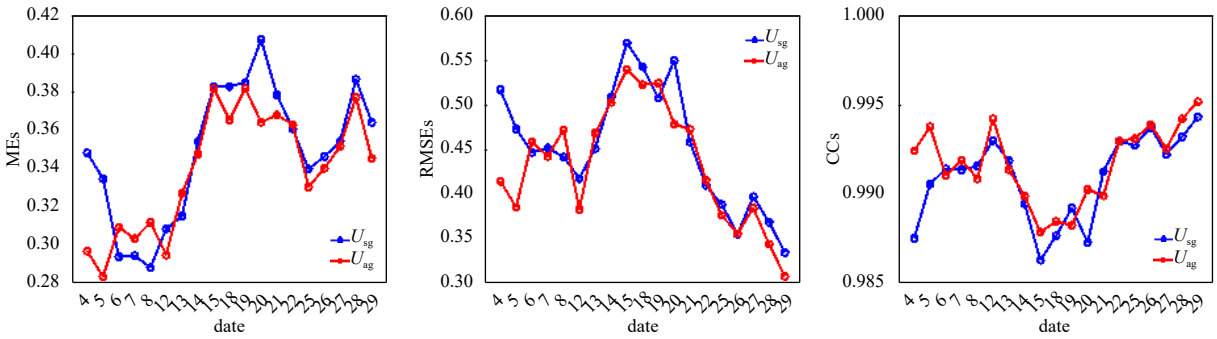

Fig. 11. The mean errors (MEs, left panels), root mean square errors (RMSEs, middle panels) and correlation coefficients (CCs, right panels) of the Kuroshio Current path locations. These indices calculated between U_{sg} and U_{ja} (red lines) and U_{ag} and U_{ja} (blue lines) in January 2018. All the days of January which is recorded in quick report maps from HOD are selected.

osio-num.html. We also thank Kara Bogus, from Liwen Bianji, Edanz Editing China (www.liwenbianji.cn/ac), for editing the English text of a draft of this manuscript.

References

Ambe D, Imawaki S, Uchida H, et al. 2004. Estimating the Kuroshio Axis South of Japan using combination of satellite altimetry and drifting buoys. Journal of Oceanography, 60(2): 375–382, doi: 10.1023/B:JOCE.0000038343.31468.fe

Arbic B K, Scott R B, Chelton D B, et al. 2012. Effects of stencil width on surface ocean geostrophic velocity and vorticity estimation from gridded satellite altimeter data. Journal of Geophysical Research: Oceans, 117(C3): C03029, doi: 10.1029/2011JC007367

CNES. 2016. SSALTO/DUACS User Handbook: (M)SLA and (M)ADT Near-Real Time and Delayed Time Products. CLS-DOS-NT-06-034

Hu Xiaomin, Xiong Xuejun, Qiao Fangli, et al. 2008. Surface current field and seasonal variability in the Kuroshio and adjacent regions derived from satellite-tracked drifter data. Acta Oceanologica Sinica, 27(3): 11–29

Hui Zhenli, Xu Yongsheng. 2016. The impact of wave-induced Coriolis-Stokes forcing on satellite-derived ocean surface currents. Journal of Geophysical Research: Oceans, 121(1): 410–426, doi: 10.1002/2015JC011082

Imawaki S, Gotoh M, Yoritaka H, et al. 1996. Detecting fluctuations of the Kuroshio axis south of Japan using TOPEX/POSEIDON altimeter data. Journal of Oceanography, 52(1): 69–92, doi: 10.1007/BF02236533

Ishikawa Y, Awaji T, Akimoto K. 1997. Global surface circulation and its kinetic energy distribution derived from drifting buoys. Journal of Oceanography, 53(5): 489–516

Lagerloef G S E, Mitchum G T, Lukas R B, et al. 1999. Tropical Pacific near-surface currents estimated from altimeter, wind, and drifter data. Journal of Geophysical Research: Oceans, 104(C10): 23313–23326, doi: 10.1029/1999JC900197

Liu Zhiqiang, Gan Jianping. 2012. Variability of the Kuroshio in the East China Sea derived from satellite altimetry data. Deep Sea Research Part I: Oceanographic Research Papers, 2012, 59: 25–36

Matsuno T, Lee J S, Yanao S. 2009. The Kuroshio exchange with the South and East China Seas. Ocean Science, 5: 303–312, doi: 10.5194/os-5-303-2009

Miyazawa Y, Kagimoto T, Guo X Y, et al. 2008. The Kuroshio large meander formation in 2004 analyzed by an eddy-resolving ocean forecast system. Journal of Geophysical Research: Oceans, 113(C10): C10015, doi: 10.1029/2007JC004226

Philipps O M. 1977. The Dynamics of the Upper Ocean. Cambridge, UK: Cambridge University Press

Qiu Bo. 2001. Kuroshio and Oyashio currents. In: Steele J H, Turekian K K, eds. Encyclopedia of Ocean Sciences. New York: Elsevier, 1413–1425

Teague W J, Jacobs G A, Ko D S, et al. 2003. Connectivity of the Taiwan, Cheju, and Korea straits. Continental Shelf Research, 23(1): 63–77, doi: 10.1016/S0278-4343(02)00150-4

Uchida H, Imawaki S. 2003. Eulerian mean surface velocity field derived by combining drifter and satellite altimeter data. Geophysical Research Letters, 30(5): 1229, doi: 10.1029/2002GL016445

Wu Kejian, Liu Bin. 2008. Stokes drift-induced and direct wind energy inputs into the Ekman layer within the Antarctic Circumpolar Current. Journal of Geophysical Research: Oceans, 113(C10): C10002, doi: 10.1029/2007JC004579